Development and implementation of continuous moment tensor scanning for offshore seismicity and tsunami early warning
Final Project Report

U.S.G.S Award Number G10AP00069
Douglas S. Dreger
University of California, Berkeley, California, 94720
Ph. (510)642-1844; Fax (510)643-5811; dreger@seismo.berkeley.edu

Introduction

In this project we implemented Kawakatsu's (1998) GridMT method for the Mendocino region to analyze offshore earthquakes, and to develop a tsunami early warning capability for the region. We introduced a modification to the method in which finite-source effects are accounted for by summing Green's functions for spatially separated points into a single point-source Green's function. This approach accounts for source finiteness of large earthquakes while maintaining the point-source approximation of the GridMT approach that enables realtime processing. We have published our results for the Mendocino region in Geophysical Research Letters (Guilhem and Dreger, 2011), and we are preparing a follow-up paper examining capabilities of the method using the strong motion data set recorded for the Tohoku-oki Mw9.0 Japan earthquake of 11 March, 2011.

Approach

GridMT

The GridMT method first proposed by Kawakatsu (1998) and implemented by Tsuruoka et al. (2009) recognizes that the linear moment tensor inversion is composed of the autocorrelation of Green's functions and cross correlations of Green's functions with observed waveforms. This cross-correlation may be obtained continuously on a streaming data set given adequate computational resources. Equation 1 gives the linear relationship between Green's functions (G), the moment tensor (M), and observed seismic waveforms (d).

$$GM = d \qquad (1)$$

The generalized inverse solution to (1) is,

$$M = (G^T G)^{-1} G^T d \qquad (2)$$

where $G^T G$ is the autocorrelation of Green's functions represented by a 6x6 matrix. This matrix and its inverse can be computed once and stored, thereby reducing processing time. $G^T d$ is the cross-correlation of Green's functions and observed waveforms, which can be computed as the data arrives. In practice we pre-compute the $(G^T G)^{-1} G^T$ matrix for an assumed velocity structure for the prescribed virtual source locations, and the locations of the stations used in the analysis. The moment tensor is then simply the cross-correlation of this inverse matrix with streaming data, and can be performed in realtime.

Tsuruoka et al. (2009) show that their GridMT method can process 7000 virtual point-sources, representing a 2.4 degree x 2.4 degree x 90 km (depth) grid sampled by a 0.1 degree laterally and 9 km in depth, in realtime on a Intel Xeon 3.06 GHz machine. They process 120 seconds of waveform data every 2 seconds monitoring a variance reduction (VR) goodness of fit parameter. When the fitting parameter exceeds a threshold (VR≥ 65%) an event is declared. The grid node with the best VR gives the location of the event, and the moment tensor and origin time of the event are determined simultaneously. They are now determining moment tensors every second for the subduction zone region of northern Japan (north of 33°) using a multi-processor distributed computing environment (e.g. http://wwweic.eri.u-tokyo.ac.jp/GRiD_MT/). Tajima et al. (2002) demonstrated that this method could be implemented in California.

Results

Implementation of GridMT in Mendocino

We have written software implementing the GridMT method of Kawakatsu (1998) and Tsuruoka et al. (2009). The software is designed to process streaming data by applying recursive filters and decimating to 1 sample per second, and performing seismic moment tensor inversions at several thousand virtual source locations every 2 seconds. The estimated VR for each virtual source solution is used to detect and locate the event. Supporting software for calculating Green's functions, preprocessing them, and constructing the $(G^TG)^{-1}G^T$ matrices has also been completed and cataloged.

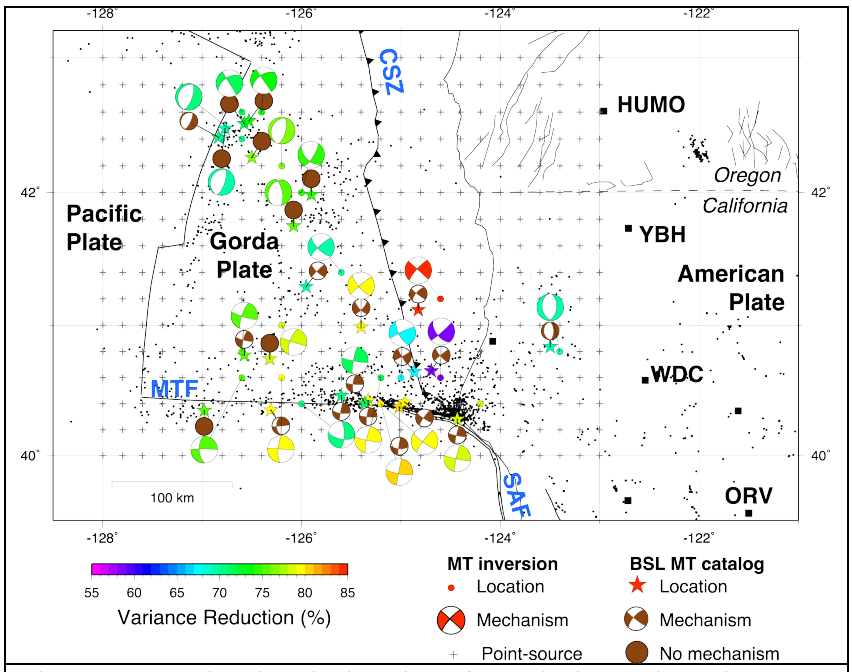

Figure 1. Map showing the location of Mendocino and Northern California seismicity (small black dots), source grid nodes (gray plusses), the four BDSN stations used in the analysis, and a comparison of GridMT moment tensors (color coded for level of fit) and catalog moment tensor solutions (brown). Fom Guilhem and Dreger, 2011.

We have developed two implementations of GridMT. The first is the standard approach for M3.5 to 7 earthquakes assuming point-source Green's functions and a filter passband of 0.02 to 0.05 Hz (e.g. Tsuruoka et al., 2009). The gray plusses in Figure 1 show the grid nodes, which are uniformly distributed every 0.2^{o} and every 3 km in depth from 5 to 38 km. There are 4992 nodes in the virtual source volume for which moment tensors are

computed every 2 seconds. This implementation is suitable for events less than magnitude 8. In Figure 1 we compare the GridMT solutions (color scaled by goodness of fit, variance reduction) and the catalog MT solutions. The stars give the catalog location and the circles show the best fitting GridMT node. The locations are generally good, however the GridMT solution can be as much as 20-30 km away from the catalog location. This is in part due to the assumed velocity structure as well as the fact that only four stations are used in GridMT for processing speed. On the other hand, the GridMT solution finds a best fit cross-correlation of complete waveforms (P and S body-waves, Love and Rayleigh surface waves) and Green's functions, and in the offshore region it may result in better locations than those based solely on P-wave arrival times. In the cases were there is a catalog moment tensor solution there is very good agreement between the GridMT and catalog results. The comparison shows that the GridMT method implemented in the realtime processing system would be capable of independently detecting, locating and determining seismic moment tensors in the offshore Mendocino region in realtime by cross-correlating low-frequency streaming waveforms with appropriate Green's functions.

The second implementation targets possible great earthquakes on the Cascadia subduction Zone (CSZ) by utilizing 100 to 200 seconds period waves, and by constructing quasi-finite-source (QFS) Green's functions that account for the spatial distribution of fault slip, rupture finiteness, and simple directivity models while still maintaining a point-source structure in the inversion. Our tests, described below, have been published in Geophysical Research Letters (Guilhem and Dreger, 2011) and demonstrate that a system can be crafted. Such a system enables the robust determination of the seismic moment tensor and the scalar seismic moment that does not saturate, and it allows these solutions to be obtained in an 8 minute time frame.

In the open ocean the velocity of tsunami propagation is approximately the square root of the product of the acceleration of gravity and the water depth. Given a water depth of 1000 m the propagation velocity is approximately 100 m/s. For the distance of the CSZ to the coast (Figure 1) open-ocean transit times for tsunami waves is approximately 6 to 20 minutes, however the actual transit time is closer to the 20 minute estimate since as the tsunami travels east the water is shallowing, reducing the deep water propagation velocity further. In 1992 a Mw7.1 thrust earthquake occurred at Cape Mendocino (Oppenheimer et al., 1993). This earthquake generated a tsunami and the earliest reported arrival was 25 minutes, and the largest recorded amplitude was due to an edge wave propagating in the near-coastal environment 3 hours after the event (Gonzales et al., 1995). A robust estimate of the fault plane solution and an unsaturated scalar seismic moment estimate determined within 8 minutes after the occurrence of a great earthquake in the CSZ could yield 10 to 20 minutes of tsunami early warning.

As discussed earlier the current system that inverts for seismic moment tensors using 20 to 50 seconds period waves will saturate for a great earthquake. Figure 2 illustrates this problem. First we simulated synthetic data for an Mw 8.2 earthquake with uniform slip on the rectangular fault surface shown in Figure 2a. The input focal mechanism is shown in red. An example of the unfiltered synthetic data and filtered versions in the 20 to 50 and 100 to 200 second passbands are shown in Figure 2b. Both filters are causal. In the 20 to 50 second passband only a fraction of the total duration of the synthetic data is modeled, and an incorrect focal mechanism (brown focal mechanism plot) is obtained. In addition the scalar moment is

grossly underestimated yielding only Mw 6.7. On the other hand in the 100-200 second passband a better reverse-style mechanism (black), and the correct scalar moment are obtained. This example also shows that for large earthquakes, there is a broad region that has higher levels of fit that correlates with the surface projection of the fault model, rather than more localized distributions that we have found for the smaller real earthquakes that we have studied (e.g. Figure 1).

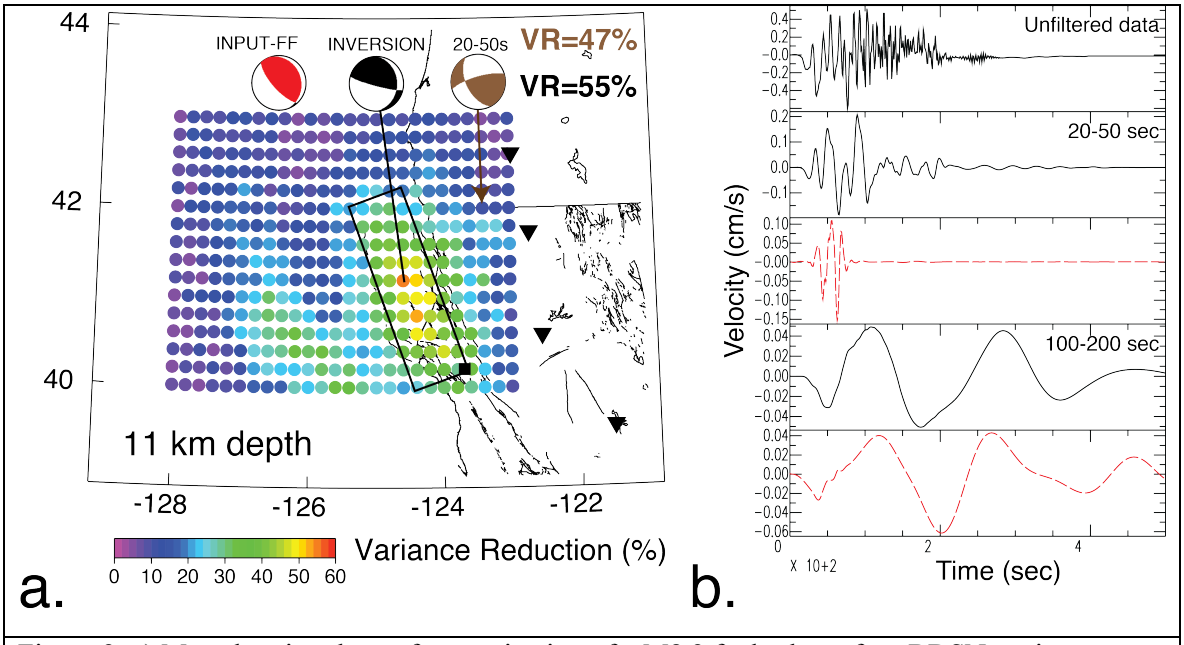

Figure 2. a) Map showing the surface projection of a M8.2 fault plane, four BDSN station (inverted triangles), and virtual source locations (circles). b) Unfiltered and filtered synthetic data (black) and synthetics (red) are compared. Note that in the 20-50 second passband only a fraction of the time series is fit, whereas in the 100-200 second passband the same point-source Green's functions can fit most of the data. From Guilhem and Dreger, 2011.

Quasi-Finite-Source (QFS) Green's functions

Although the point-source results in the very long-period passband were reasonable when using stations that are located 100 to 300 km from a 250 km long fault, we found that the stations as used in our tests were located in the near-field, and therefore subject to the effects of finite-fault rupture. To account for finite-source effects we developed the QFS Green's function method in which Green's functions from spatially separated points are summed to form a new composite Green's function at a central reference point. The GridMT approach is then performed using these modified Green's functions. Furthermore, it is also possible to consider the effects of source directivity in the construction of the QFS Green's functions.

To illustrate the concept, the example in Figure 3a shows a variable slip rupture model superimposed on the grid. The rupture is unilateral from south to north. In this example a QFS Green's function is constructed by summing the east-west, north-south and vertical component fundamental fault Green's functions for virtual sources located at (4,8), (3,7) and (2,6), and then referencing the QFS Green's functions to the central point.

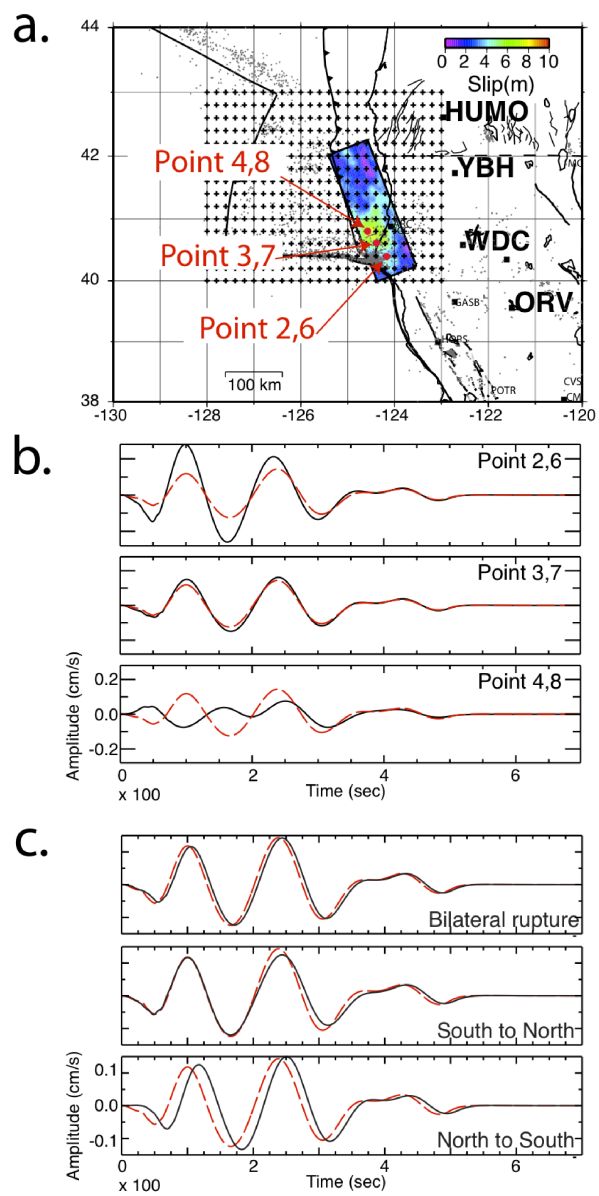

Figure 3 a) Map of the slip model of a synthetic M8.1 earthquake (rectangle). Arrows point to the three grid-points considered in the generation of quasi-finite-source GFs. b) Synthetic EW components at WDC computed for the three different grid-points (black, solid traces) compared to the quasi-finite-source GF computed using the three selected grid points (red, dashed traces). c) Directivity in the quasi-finite-source GF (black, solid traces) compared to the GFs without directivity of b) (red, dashed traces). From Guilhem and Dreger, 2011.

Figure 3b compares the QFS Green's functions (red) with the individual virtual source Green's functions (black). Over the 63 km span of these three virtual sources there are significant changes in the waveform (i.e. amplitudes and wave polarities) of each point-source Green's function owing to the differences in the effective radiation pattern at the respective azimuths to the recording station. Figure 3c shows how the QFS Green's functions vary if different directivity models are considered (i.e. bilateral or unilateral). With this formalism it is possible to construct a set of QFS Green's functions that sample different sections on the subduction

zone interface as well as kinematic rupture scenarios such as south-to-north or north-to-south rupture. These QFS Green's functions can then be treated as point-source Green's functions in the GridMT algorithm enabling rapid source parameter estimation.

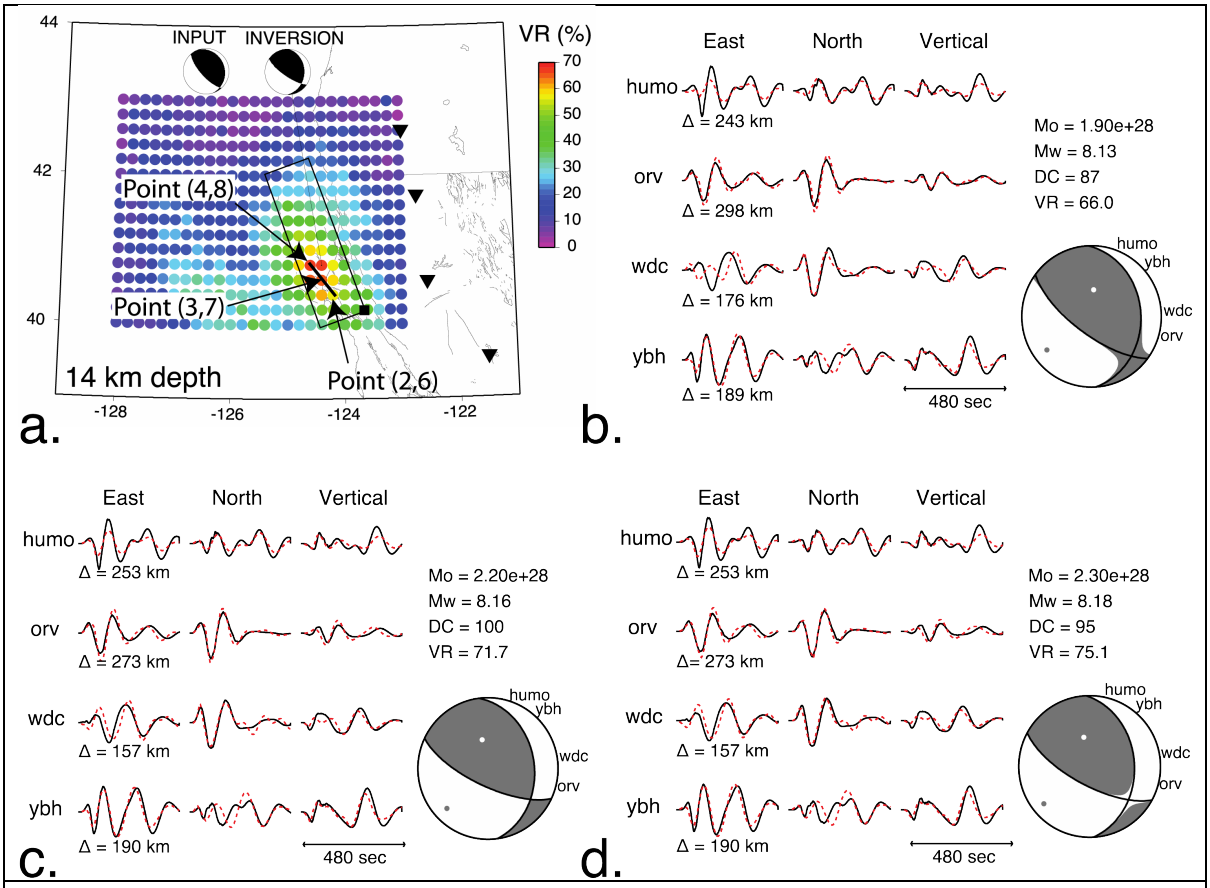

Figure 4. a) Map of the best VRs at 14 km depth obtained for a point-source moment tensor inversion for a synthetic M8.2 earthquake (rectangle). The best mechanism (top, right) is compared to the input mechanism (top, left). Arrows point to the points that are considered in the multi-point source inversion. b) Best moment tensor solution obtained at Point (3,7). c) Moment tensor solution for the multi-point source inversion (no directivity). d) Moment tensor solution for the multi-point source inversion with a northward directivity. From Guilhem and Dreger, 2011.

In Figure 4 we compare inversion results for the cases of the point-source, QFS Green's functions without directivity, and QFS Green's functions with directivity. Figure 4a shows the goodness of fit parameter (VR) observed over the grid for a source depth of 14 km. The best fitting point-source solution (Figure 4b) is located in the region of the peak slip shown in Figure 3. The best fit for the single point-source case is 66%, which is better than the uniform slip case shown in Figure 2 due to the concentration of slip into a primary asperity in this variable slip case. In Figure 4c the solution obtained using QFS Green's functions without directivity is compared and we show that the fit improves significantly to 71.7%. In Figure 4d the QFS Green's functions case with northward directivity result in a variance reduction of 75%. The QFS Green's functions case with an incorrect north to south directivity yields only 66.7% fit. In the point-source cases, the scalar moment is slightly under-predicted: Mw 8.1

versus 8.2. In the two cases with QFS Green's functions the correct moment is recovered, and the example suggests that the information regarding the rupture directivity may be recoverable.

March 11, 2011 Tohoku-oki Mw9.0 earthquake

On March 11, 2011 a devastating earthquake with a magnitude of 9.0 struck Japan. Studies of the finite-source process indicate that slip in the shallow part of the subjection zone may have reached as much as 55 m. This large, shallow fault offset led to sea floor deformation resulting in a great tsunami that swept the east coast of northern Honshu. This event was well recorded by the NIED K-net of strong motion instruments that recorded the earthquake onscale with the largest accelerations exceeding 2g, but importantly they also recorded the long-period accelerations that may be used by a regional moment tensor based tsunami early warning system as we have proposed.

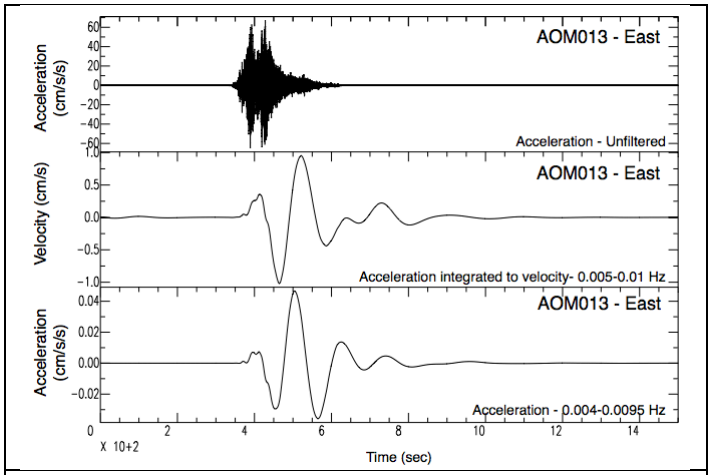

Figure 5. Waveform comparison of the East component of station AOM013. Top: raw, unfiltered strong-motion data. Middle: top seismogram integrated to velocity and bandpass filtered between 0.005 and 0.01 Hz. Bottom: top seismogram bandpass filtered between 0.004 and 0.0095 Hz.

In Figure 5 representative unfiltered accelerations and filtered velocity and accelerations are compared. These data show that the deployed accelerometers have recorded the very low frequency (0.004 to 0.01 Hz), 100 to 250 seconds period accelerations with exceptional signal to noise. As shown by Guilhem and Dreger (2011), and described above this passband should be suitable for the unbiased recovery of the seismic moment tensor and scalar seismic moment using the GridMT method and the QFS Green's function approach. We have collected the strong motion data from the K-net and have tested the method examining the sensitivity of the approach to the passband, data type (velocity or acceleration), and station configuration.

The relative compactness of the rupture in the case of the Tohoku-oki earthquake compared to earthquakes of similar magnitude helps for the high VRs obtained using single-point-source GFs with stations located near the rupture zone. Our results show the need to filter the seismic waveforms at longer periods in order to recover the source characteristics of a large earthquake. Nonetheless, for great earthquakes, Guilhem and Dreger (2011) proposed the use of QFS GFs to account for the rupture finiteness at these distance ranges. We tested a series of QFS GFs inversions that represent to some extent the extended dimensions of the rupture to those in which we add or not add a directivity effect (Figure 6). We summed three, four, and five grid points to create a series of rupture scenarios with elongated and square QFS GFs geometries. Complexities in the construction of the QFS GFs are possible to implement but they require a priori knowledge of the rupture, which is not known nor well predicted prior to earthquake

occurrence. Here, we only considered GFs at the slab depth and we search for the best VR every 2 seconds with a reduced number of grid inversions compared to what was computed with the single-point-source GFs. This corresponds to a greatly reduced number of inversions per grid compared to the inversion scheme employed for smaller earthquakes in Japan (i.e. less than 7,000 per grid) and in northern California (nearly 5,000) for which regular three-dimensional grids are used (Tsuruoka et al., 2009; Guilhem and Dreger, 2011).

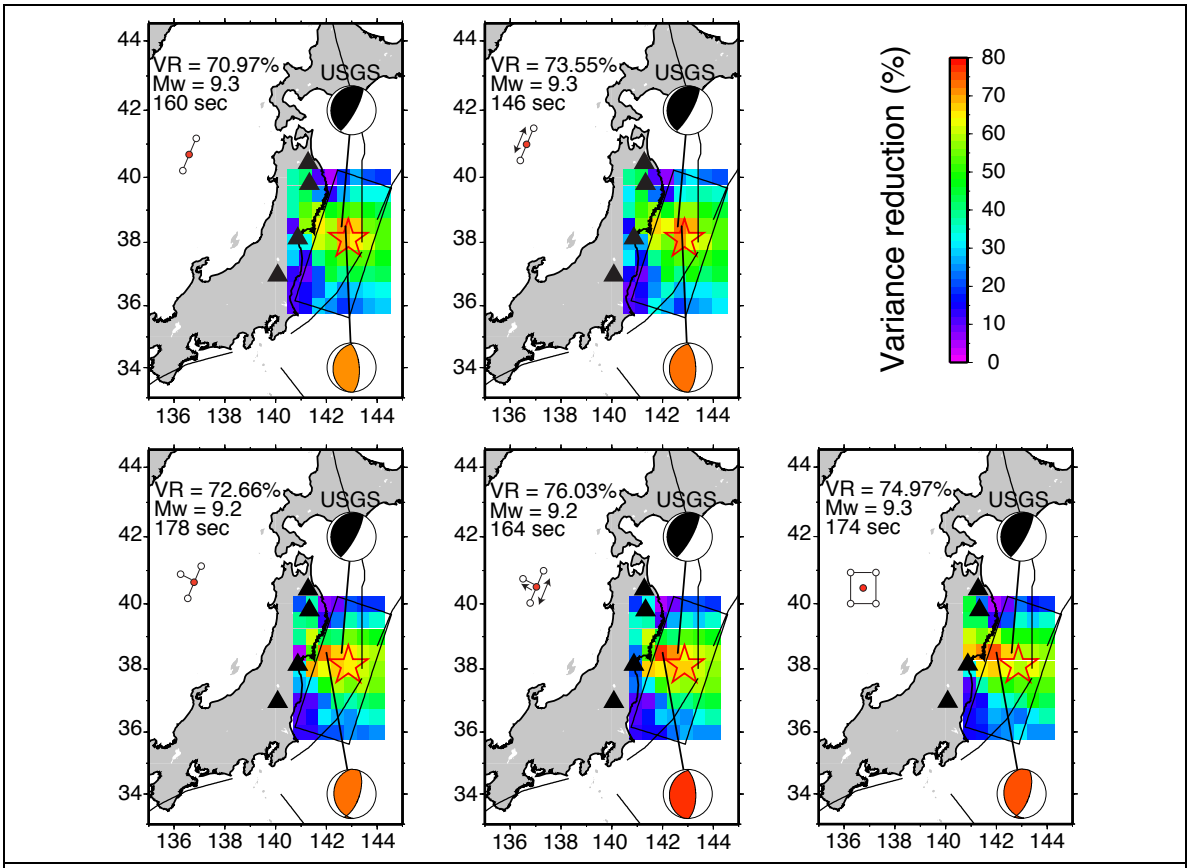

Figure 6: GridMT results for acceleration records at 4 stations at slab depth using different quasi-finite-source GFs shown by the white and red dots representing the combination of point sources (drawn to scale) with or without directivity (arrows). The red dots are considered as references for the rotations from transverse / radial components to east / north components and for the moment tensor inversions.

We find that the use of this limited number of QFS GFs applied to strong-motion records allow the rapid detection of the M9 Tohoku-oki earthquake with VRs exceeding 70% and reaching a maximum of 75 % (Figure 6). The mechanism, location, and origin times are generally well retrieved and are similar to those obtained with the single-point-source GFs. In addition, when using a bilateral rupture we better recover the source parameters of the earthquake (i.e. larger VR) as we better represent the original rupture mode of the mainshock. Because this approach is less computatively intensive with the restricted number of inversions required, it is possible to invert simultaneously for several rupture styles (i.e. multiple shapes with or without directivity) in order to better reflect anticipated ruptures in the region of interest. Furthermore, Figure 6 also demonstrates that very simple rupture scenarios with only three points can be used for the rapid characterization of this earthquake, which is similar to results published by

Guilhem and Dreger (2011) when testing the approach on large earthquakes along the CSZ with longer ruptures.

The magnitude of the event is however found to be larger than expected (i.e. 9.3 instead of 9.0). This can result from the use of summed GFs with large source time functions, and/or uncertainties in the velocity model affecting the GFs and consequently the source parameters. By reducing the source duration in the GFs, the estimated moment of the earthquake is reduced. With the reduced number of calculations it will also be able to test cases with different source time durations. Nevertheless, these results show that at long periods it is possible to detect and characterize a mega-thrust earthquake with limited source inversions and with limited knowledge on the regional structure, earthquake rupture and duration. This information could be known within 8 minutes after the occurrence of the earthquake if robust telemetry and hardened processing centers are employed. The arrival time of the devastating tsunami depends on location along the coast but generally the largest waves arrived between 20 to 30 minutes following the earthquake (Japan Meteorological Agency Preliminary Report). Thus as much as ten minutes and for some regions more warning is possible in the near-field of great earthquakes. Finally, additional tests are required for a better calibration of the filters and GFs for each region of interest but as shown the method can help to rapidly provide, within minutes after a large earthquake, useful onscale information that can be utilized for tsunami early warning.

References

Guilhem, A., and D. S. Dreger (2011). Rapid detection and characterization of large earthquakes using quasi-finite-source Green's functions in continuous moment tensor inversion, Geophys. Res. Lett., Vol. 38, L13318, doi:10.1029/2011GL047550, 2011

Gonzalez, F. I., K. Satake, E. F. Boss, and H. O. Mofjeld (1995). Edge wave and non-trapped models of the 24 April 1992 Cape Mendocino Tsunami, PAGEOPH, Vol. 144, 409-426.

Kawakatsu, H., (1998) On the realtime monitoring of the long-period seismic wavefield., Bull. Earth. Res. Inst., 73, 267-274.

Oppenheimer, D., Beroza, G., Carver, G., Dengler, L., Eaton, L., Gee, L., González, F., Jayko, A., Li, W. H., Lisowski, M., Magee, M., Marshall, G., Murray, M., McPherson, R., Romanowicz, B., Satake, K., Simpson, R., Somerville, P., Stein, R. and Valentine, D. (1993), The Cape Mendocino, California, Earthquakes of April 1992: Subduction at the Triple Junction, Science, 261, 433-438.

Tajima, F., C. Megnin, D. Dreger, B. Romanowicz (2002) Feasibility of real-time broadband waveform inversion for simultaneous moment tensor and centroid location determination, Bull. Seism. Soc. Am., vol.92, no.2, pp.739-750.

Tsuruoka, H., H. Kawakatsu, and T. Urabe (2009), GRiD MT (grid-based real-time determination of moment tensors) monitoring the long-period seismic wavefield, Physics of the Earth and Planetary Interiors, 175, 8-16, doi:10.1016/j.pepi.2008.02.014

Appendix

Guilhem and Dreger (2011) as published in Geophysical Research Letters.

Rapid detection and characterization of large earthquakes using quasi-finite-source Green's functions in continuous moment tensor inversion

Aurélie Guilhem[1] and Douglas S. Dreger[1]

Received 23 March 2011; revised 25 May 2011; accepted 25 May 2011; published 15 July 2011.

[1] Large earthquakes along subduction zones have the potential to generate tsunamis along local coasts, as well as traveling far across oceans. By continuously inverting for moment tensors we show that it is possible with a single procedure to automatically detect, locate and determine source parameters of any earthquake, from magnitude 3.5 to larger than 8 located in both the near- and far-field. We find that the detection and characterization of large earthquakes is improved when quasi-finite-source Green's functions are used in a point-source moment tensor approach as they represent to some extent the rupture's finiteness and directivity. Solutions can be obtained within several minutes after the origin time of the earthquake, and could therefore be used as part of a near-source tsunami early warning system, capable of providing tens of minutes of possible warning depending on the distance of the earthquake rupture from the coast. **Citation:** Guilhem, A., and D. S. Dreger (2011), Rapid detection and characterization of large earthquakes using quasi-finite-source Green's functions in continuous moment tensor inversion, *Geophys. Res. Lett.*, *38*, L13318, doi:10.1029/2011GL047550.

1. Introduction

[2] As recently demonstrated by the 2004 magnitude (Mw) 9.0 Sumatra, the 2010 Mw8.8 Chile and the 2011 Mw9.0 Japan seismic events, great subduction zone earthquakes are capable of triggering devastating, high-fatality tsunamis in their near field, in addition to producing intense local ground shaking [*Bryant*, 2001; *Hirshorn and Weinstein*, 2009]. With increasing continuously recording seismic networks, current efforts provide earthquake and tsunami early warnings within 5 to 10 min after the origin time [*Lomax and Michelini*, 2009]. Current procedures focus on earthquake location, depth, magnitude, and slowness [*Hirshorn and Weinstein*, 2009]. But initial tsunami early warning statements are commonly issued without knowing the focal mechanism of the earthquake, which has first order importance, together with the magnitude and focal depth, on the excitation of tsunami waves.

[3] *Kanamori and Rivera* [2008] proposed the use of the fast-propagating long-period W-phase in an automated manner for moment tensor inversions. Complete earthquake source parameters can be known within 20 minutes following the earthquake origin time [*Kanamori and Rivera*, 2008] and are now computed at the Pacific Tsunami Warning Center as well as in Japan [*Tsuruoka et al.*, 2009a]. However, it remains limited in its ability to provide useful near-field tsunami early warnings because of its intrinsic time delay [*Lay et al.*, 2005]. Considering datasets closer to the earthquake rupture may improve the processing time for the source characterization by putting a lower distance bound on the useable data. But the rupture dimensions for M8+ events violate the point-source assumptions applied in moment tensor inverse methods. Even if finite-source inversions solve this problem, their realtime implementations are computationally demanding [*Dreger and Kaverina*, 2000; *Dreger et al.*, 2005]. Also, while it is possible to rapidly obtain solutions within a 20 min time frame for M6+ offshore events [*Dreger*, 2010] the scaling of finite-source model dimensions for great earthquakes precludes their implementation in realtime. On the other hand, *Kawakatsu* [1998] proposed a realtime approach to automatically detect, locate and determine the source parameters of earthquakes occurring within a predefined region by computing moment tensors at each point of a grid from continuously streaming long-period (>10 sec) waveform data. With a limited number of stations and assuming a point-source representation, this method gives correct results in terms of detection and source characterization of up to M7 earthquakes offshore Japan [*Tsuruoka et al.*, 2009b].

[4] Here, we present an adapted version of *Kawakatsu*'s [1998] method, focusing on the most seismically active region of northern California: the Mendocino Triple Junction (MTJ), where small to potentially tsunamigenic earthquakes occur. For major earthquakes (M8+), we propose a point-source moment tensor inversion that takes into account the finiteness of the rupture zone by constructing quasi-finite-source Green's functions (GFs). It becomes possible to monitor all M > 3.5 earthquakes with a direct procedure that autonomously detects, locates, and computes source parameters. This is performed using a single step procedure in contrast to the standard cascade-type analysis currently employed in northern California [*Gee et al.*, 2003].

2. Data and Method

[5] With approximately 80 earthquakes with magnitude larger than 3 every year, the MTJ is known as the most seismically active region in northern California [*Oppenheimer*, 2007]. Its seismicity is mostly located offshore: along the Mendocino Transform Fault (MTF), within the highly deformed Gorda plate, and along the Cascadia Subduction Zone (CSZ) (Figure 1). Paleoseismic evidence of great earthquakes along the CSZ [*Atwater*, 1987], including radiocarbon dating and several offshore turbidite

[1]Berkeley Seismological Laboratory, University of California, Berkeley, California, USA.

Copyright 2011 by the American Geophysical Union.
0094-8276/11/2011GL047550

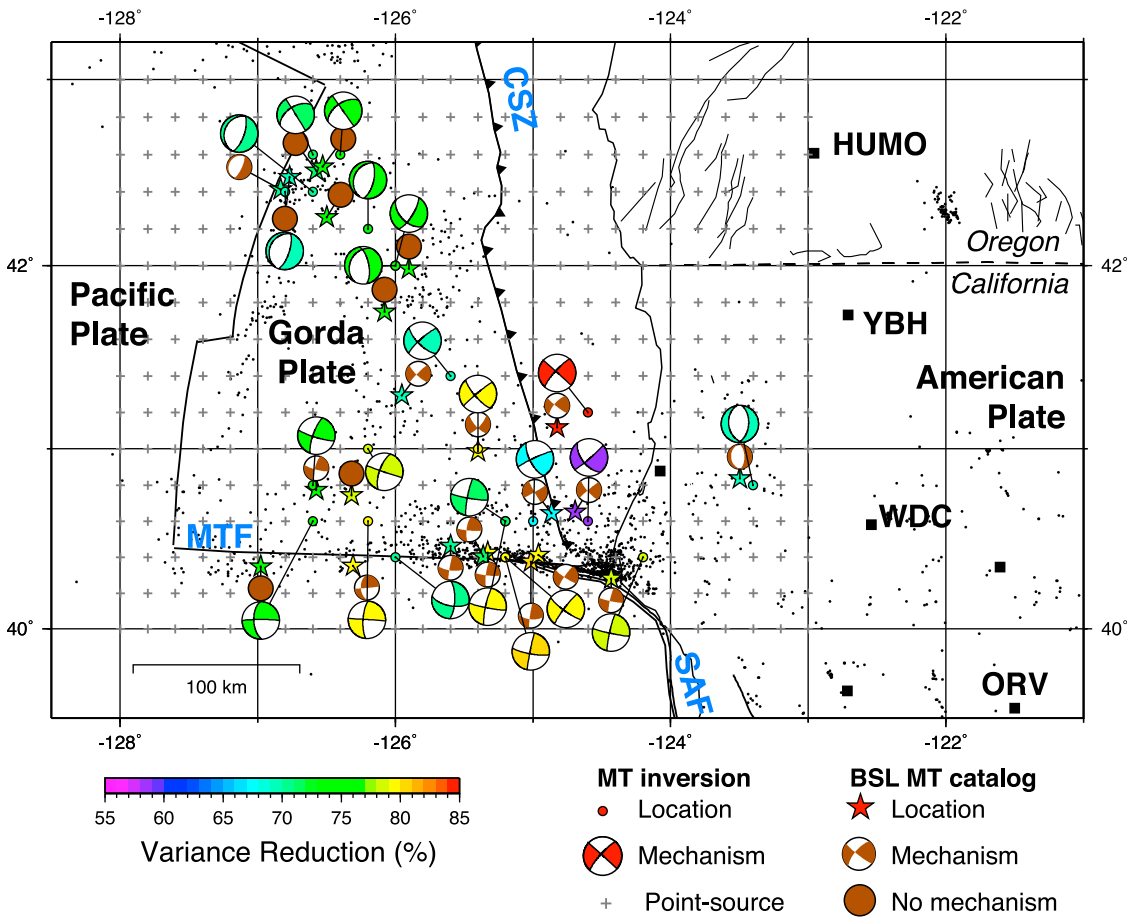

Figure 1. Map of the Mendocino Triple Junction region showing the grid of point sources (crosses). The four seismic stations used are HUMO, ORV, WDC and YBH. Black dots show the regional seismicity (M3+) since 1990. The studied events are shown in brown for the catalog solutions and are color-coded by the VR for the inversion solutions. CSZ, MTF, and SAF mark the Cascadia subduction zone, the Mendocino transform fault, and the San Andreas fault, respectively.

episodes of deformation in the last 2000 years [*Clarke and Carver*, 1992], indicate that the CSZ is capable of multiple M8+ earthquakes, as large as M9 [*Goldfinger et al.*, 2008; *Satake et al.*, 1996; *Heaton and Hartzell*, 1987].

[6] In northern California, current realtime earthquake monitoring is performed sequentially by the U.S. Geological Survey at Menlo Park and the Berkeley Seismological Laboratory [*Gee et al.*, 2003]. Because seismic stations are located onshore, poor azimuthal coverage of the seismic wave radiation patterns often leads to difficulties in detecting and locating events, and thus in determining their full source parameters. There is a need to implement a system that will automatically characterize earthquake sources and will not depend on the successful completion of multi-stage processing.

[7] *Kawakatsu* [1998] proposed to continuously invert the long period seismic wavefield (>10 sec) for moment tensors at grid points representing virtual sources distributed over a region. At each station, the data d are represented as the convolution of the GF tensor, G, describing the wave propagation between the source and the receiver, and the moment tensor components m of the source:

$$d = G \cdot m \tag{1}$$

[8] The least-square solution for the moment tensor can be obtained:

$$M = \left(G^T G\right)^{-1} G^T d \tag{2}$$

where the $(G^TG)^{-1}G^T$ matrix for each point-source can be computed in advance knowing a priori the grid distribution and the set of pre-selected seismic stations. The multiplication of this matrix with streaming data can be performed continuously as soon as the data arrives at a central site. Earthquake detection is given when the variance reduction (VR) exceeds a detection threshold:

$$VR = \left[1 - \sum_i \sqrt{(data_i - synth_i)^2} \Big/ \sum_i \sqrt{data_i^2}\right] \times 100 \tag{3}$$

where *data*, and *synth* are the discrete data and GF time series, respectively, and the summation is performed for all stations and components.

[9] We propose to implement a moment tensor grid search covering the MTJ using four broadband seismic stations of the Berkeley Digital Seismic Network and nearly 5,000 virtual sources located every 0.2° in latitude and longitude and every 3 km in depth, between 5 and 38 km (Figure 1).

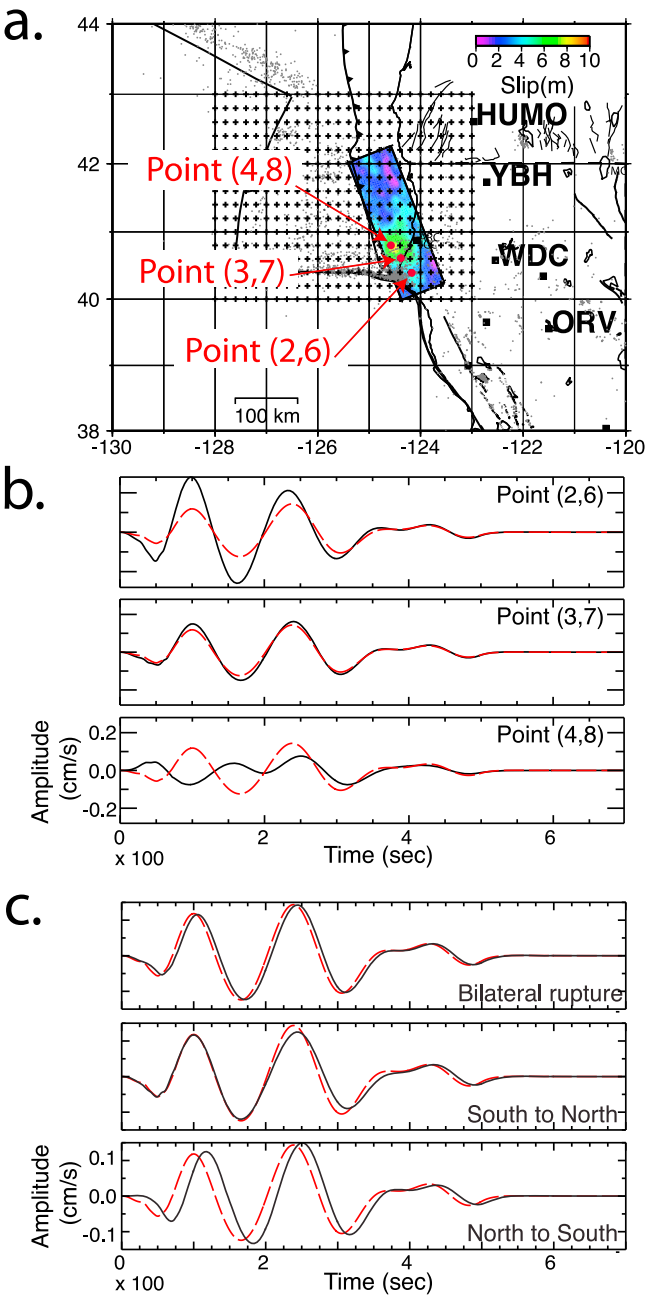

Figure 2. (a) Map of the slip model of a synthetic M8.1 earthquake (rectangle). Arrows point to the three grid-points considered in the generation of quasi-finite-source GFs. (b) Synthetic EW components at WDC computed for the three different grid-points (black, solid traces) compared to the quasi-finite-source GF computed using the three selected grid points (red, dashed traces). (c) Directivity in the quasi-finite-source GF (black, solid traces) compared to the GFs without directivity of Figure 2b (red, dashed traces).

We suggest running in parallel a system for small to moderate earthquakes and a second one for large (M8+) earthquakes along the CSZ (see auxiliary material).[1] For M3.5–7 earthquakes, the inversion of 380 sec of data is performed every 2 seconds after filtering the seismic wavefield between 20 and 50 sec. This allows sufficient propagation time for the full seismic waveforms to reach the seismic stations. For the second system, we invert a longer record (i.e., 480 sec) and filter the data between 100 and 200 sec (Figure S1). In addition, for large earthquakes, the source time function becomes a significant parameter that needs to be considered. We choose to include an 84-sec source time function to the GFs corresponding to the synthetic M8.2 earthquake we present here (Figures 2 and S1), however it is possible to consider several different source time function durations within a reasonable range for scenarios targeting specific types of events (e.g., Mw 8.0, 8.5, 9.0, etc.).

[10] For M8+ earthquakes along the CSZ, we propose to invert for moment tensors only at the grid points that are distributed in the slab. This significantly lowers the number of calculations and permits us to focus on the most hazardous region of the grid. It is then possible to consider earthquake scenarios in advance and to invert for them in realtime. However, this grows into a near-field problem in which the stations are sensitive to different parts of the overall rupture. We propose here to employ quasi-finite-source adjusted GFs where GFs of n grid points are averaged in advance to generate composite GFs, G_{tot}, that take into account the source-receiver back-azimuth and thereby the effective radiation patterns of each component (Figure 2):

$$G_{tot}(t) = \sum_{i=1}^{n} G_i(t) \Big/ n \tag{4}$$

[11] The prefixed number of points n has an effect on the complexities of the pre-defined earthquake scenarios considered in the realtime inversions. Directivity can also be pre-included in the composite GFs, giving constraints on the nature of finite rupture (i.e., unilateral or bilateral) (Figure 2):

$$G_{tot}(t) = \left[G_1(t) + \sum_{i=2}^{n} G_i(t) \cdot \left(\frac{\Delta_{1-n}}{v_r} \right) \right] \Big/ n \tag{5}$$

where Δ_{1-n} is the distance between Source 1 (reference source) and Source n and v_r is the rupture velocity. The moment tensor inversion itself is performed assuming a point-source analysis method, which maintains the computational speed. One of the point-sources of the composite GF is considered as a reference because information about the corresponding azimuths between the selected grid-point and the seismic stations is needed to rotate the GFs into the East, North and vertical components for the realtime inversion.

3. Results

[12] We test the concept on M4 to M7.1 earthquakes (Figure 1 and Table S1). The solutions obtained using a 1 D velocity model agree well with the Berkeley moment tensor catalog solutions confirming that this system is suitable for implementation in the MTJ region. However, the 20–50 sec inversions of 380 sec long records for a synthetic M8.2 reverse event with uniform slip fail to recover the earthquake parameters, yielding only Mw 6.7 and a poor fit, VR = 47% (Figure S1). Because of the narrow band processing, the point-source inversion only fits a small part of the record and is not sensitive to the total seismic moment. The source

[1]Auxiliary materials are available in the HTML. doi:10.1029/2011GL047550.

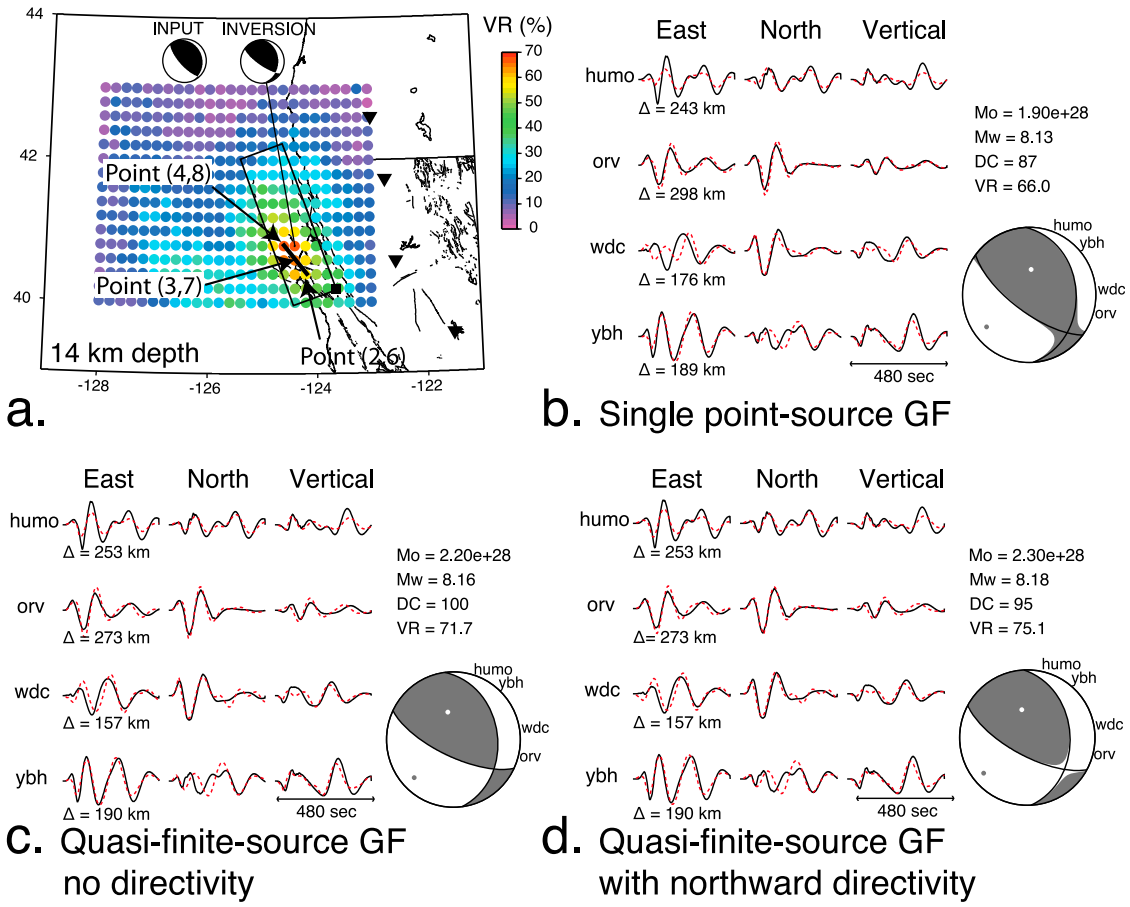

Figure 3. (a) Map of the best VRs at 14 km depth obtained for a point-source moment tensor inversion for a synthetic M8.2 earthquake (rectangle). The best mechanism (top right) is compared to the input mechanism (top left). Arrows point to the points that are considered in the multi-point source inversion. (b) Best moment tensor solution obtained at Point (3,7). (c) Moment tensor solution for the multi-point source inversion (no directivity). (d) Moment tensor solution for the multi-point source inversion with a northward directivity.

corner frequency of the event (~0.011 Hz) is indeed lower than the frequency band considered. In contrast, the 100–200 sec passband works better (VR = 54.6% in Figure S1) and gives a point-source location near the fault centroid, the correct Mw and focal mechanism. Similar results are also obtained for a variety of slip models (Mw8.2 and 8.4) using a single point-source moment tensor inversion with point-source GFs (Figures 3a, 3b, and S2). As Figure 3 shows, the best solution obtained for a synthetic M8.2 earthquake with variable slip is found within the rupture segment near the centroid. We find that more realistic variable slip distributions are better represented by a point-source assumption at longer periods as proposed by *Fukuyama and Dreger* [2000].

[13] We show that it is possible to improve the fit between the synthetics and the data (Figure 3c) after simultaneously summing the GFs of several grid points centered on the event centroid. Figure 3d shows that, by considering a northward rupture in the composite GFs and a rupture velocity of 3 km/sec, the corresponding earthquake solution has a larger VR and better estimates the focal parameters (Table S2). Similar results are obtained for a M8.4 synthetic seismic event, which presents an extended rupture (i.e., 480 km) and two major slip areas (Figure S2). This method permits raising the detection level of large earthquakes and allows us to obtain more precise source parameters (Table S2), by considering a range of quasi-finite-source Green's functions for different directivity scenarios and source time duration.

4. Discussion and Conclusion

[14] We show that it is possible to detect and characterize the seismic activity of the MTJ region using an algorithm that performs moment tensor inversions using streaming waveform data. The powerful addition of quasi-finite-source GFs enables better definition of the centroid location, the correct source mechanism and magnitude of large earthquakes. Used in a point-source formulism, they allow more rapid detection of major events and more precise determination of their source parameters than is likely to be available using standard processing systems. This approach may enable applications for tsunami early warning in the near-field of large coastal earthquakes. Detections from the automated moment tensor inversion can be as fast as the length of the inverted seismic records. Complete earthquake information is retrieved about 6 minutes after a M4-7 earthquake and 8 minutes after a M8+ earthquake. To this time, data telemetry latency (~2 sec) and a negligible ($\ll$1 sec) delay for filtering and resampling need to be added as well as

a few tens of seconds to assess fit and determine a maximum in the VR [*Tsuruoka et al.*, 2009b].

[15] In the open ocean, the velocity of tsunami propagation is proportional to the water depth. Depending on the distance of the area of uplift from the coast, the open-ocean transit times for tsunami waves may be about 6 to 20 minutes. However, the actual transit time is likely to be closer to 20 minutes due to decreasing water depth, and as reported after an Mw7.1 earthquake in 1992 that occurred at Cape Mendocino [*Oppenheimer et al.*, 1993]. Its largest amplitudes, from an edge wave, arrived 3 hours after the event [*Gonzalez et al.*, 1995]. The devastating tsunami waves following the 2011 Mw9.0 Japan earthquake arrived about 20–30 minutes after the rupture (Japan Meteorological Agency, The 2011 off the Pacific coast of Tohoku earthquake, 2011, available at http://www.jma.go.jp/jma/en/2011_Earthquake.html). The method we propose may allow for tens of minutes of warning in the near-field.

[16] Strong motion data of the 2011 M9.0 Japan earthquake reveals that 100–200 sec accelerations can be recorded with high signal-to-noise levels with modern instrumentation (Figure S3). After adapting G. Shao et al.'s (Preliminary result of the March 11th, 2011 Mw9.1 Honshu earthquake, 2011, available at http://www.geol.ucsb.edu/faculty/ji/big_earthquakes/2011/03/0311_v3/Honshu.html) slip model of the M9.0 Japan event for the MTJ region, we find good detection and characterization of the earthquake with VRs up to 85% (Figures S3 and S4). Finally, seismic instrumentation could clip from the strong shaking of a large local/regional earthquake. One or several near-field stations could also be rendered non-operational at the time of the earthquake affecting the algorithm performance. Overcoming this issue is possible by using secondary seismic stations or only a subset of the stations. However this could affect the VRs and lead to a non-detection (Figures S5 and S6). High-rate continuous GPS data could also provide on-scale observations for even the largest earthquakes [*Larson et al.*, 2003; *Avallone et al.*, 2011]. Using adequately calibrated velocity models and a proper grid distribution, this grid search approach can be implemented to include both seismic and geodetic datasets in any region that experiences intense and potentially tsunamigenic seismic activity.

[17] **Acknowledgments.** Supported by the U.S. Geological Survey through external award G10AP00069. We thank Robert Uhrhammer, GRL editor Ruth Harris, reviewer Barry Hirshorn and an anonymous reviewer for their constructive advices. Strong motion data of the 2011 M9.1 Japan earthquake from the K-NET, National Research Institute for Earth Science and Disaster Prevention (NIED). Berkeley Seismological Laboratory contribution 11-02.

References

Atwater, B. F. (1987), Evidence for Great Holocene earthquakes along the outer coast of Washington State, *Science*, *236*, 942–944, doi:10.1126/science.236.4804.942.

Avallone, A., et al. (2011), Very high rate (10 Hz) GPS seismology for moderate-magnitude earthquakes: The case of the Mw6.3 L'Aquila (central Italy) event, *J. Geophys. Res.*, *116*, B02305, doi:10.1029/2010JB007834.

Bryant, E. (2001), *Tsunami: The Underrated Hazard*, 350 pp., Cambridge Univ. Press, New York.

Clarke, S. H., and G. A. Carver (1992), Late Holocene tectonics and paleoseismicity, southern Cascadia Subduction zone, *Science*, *255*(5041), 188–192, doi:10.1126/science.255.5041.188.

Dreger, D. S. (2010), January 10, 2010 Mw6.5 Gorda Plate earthquake: Automated finite-source modeling, annual report, Berkeley Seismol. Lab., Berkeley, Calif. [Available at http://seismo.berkeley.edu/annual_report/ar09_10/node23.html.]

Dreger, D., and A. Kaverina (2000), Seismic remote sensing for the earthquake source process and near-source strong shaking: A case study of the October 16, 1999 Hector Mine earthquake, *Geophys. Res. Lett.*, *27*, 1941–1944, doi:10.1029/1999GL011245.

Dreger, D. S., L. Gee, P. Lombard, M. H. Murray, and B. Romanowicz (2005), Rapid finite-source analysis and near-fault strong ground motions: Application to the 2003 Mw 6.5 San Simeon and 2004 M-w 6.0 Parkfield earthquakes, *Seismol. Res. Lett.*, *76*(1), 40–48, doi:10.1785/gssrl.76.1.40.

Fukuyama, E., and D. Dreger (2000), Performance test of an automated moment tensor determination system for the future "Tokai" earthquake, *Earth Planets Space*, *52*, 383–392.

Gee, L., D. Neuhauser, D. Dreger, M. Pasyanos, R. Uhrhammer, and B. Romanowicz (2003), The Rapid Earthquake Data Integration System, in *International Handbook of Earthquake and Engineering Seismology*, *Int. Geophys. Ser.*, vol. 81, pp. 1261–1273, Academic, Amsterdam.

Goldfinger, C., et al. (2008), Late Holocene rupture of the northern San Andreas Fault and possible stress linkage to the Cascadia Subduction Zone, *Bull. Seismol. Soc. Am.*, *98*, 861–889, doi:10.1785/0120060411.

Gonzalez, F. I., K. Satake, E. F. Boss, and H. O. Mofjeld (1995), Edge wave and non-trapped models of the 24 April 1992 Cape Mendocino Tsunami, *Pure Appl. Geophys.*, *144*, 409–426, doi:10.1007/BF00874375.

Heaton, T. H., and S. H. Hartzell (1987), Earthquake hazards on the Cascadia Subduction Zone, *Science*, *236*, 162–168.doi:10.1126/science.236.4798.162.

Hirshorn, B., and S. Weinstein (2009), Earthquake source parameters, in *Encyclopedia of Complexity and Systems Science*, Pt. 5, pp. 2657–2676, doi:10.1007/978-0-387-30440-3_160.

Kanamori, H., and L. Rivera (2008), Source inversion of W phase: Speeding up seismic tsunami warning, *Geophys. J. Int.*, *175*, 222–238, doi:10.1111/j.1365-246X.2008.03887.x.

Kawakatsu, H. (1998), On the realtime monitoring of the long-period seismic wavefield, *Bull. Earthquake Res. Inst. Univ. Tokyo*, *73*, 267–274.

Larson, K. M., P. Bodin, and J. Gomberg (2003), Using 1 Hz GPS data to measure deformations caused by the Denali Fault earthquake, *Science*, *300*, 1421–1424, doi:10.1126/science.1084531.

Lay, T., et al. (2005), The Great Sumatra-Andaman earthquake of 26 December 2004, *Science*, *308*, 1127–1133, doi:10.1126/science.1112250.

Lomax, A., and A. Michelini (2009), Tsunami early warning using earthquake rupture duration, *Geophys. Res. Lett.*, *36*, L09306, doi:10.1029/2009GL037223.

Oppenheimer, D. (2007), Mendocino Triple Junction offshore northern California, Woods Hole Sci. Cent., U.S. Geol. Surv., Woods Hole, Mass. [Available at http://woodshole.er.usgs.gov/operations/obs/rmobs_pub/html/mendocino.html.]

Oppenheimer, D., et al. (1993), The Cape Mendocino, California, earthquakes of April 1992: Subduction at the Triple Junction, *Science*, *261*, 433–438, doi:10.1126/science.261.5120.433.

Satake, K., K. Shimizaki, Y. Tsuji, and K. Ueda (1996), Time and size of a giant earthquake in Cascadia inferred from Japanese tsunami records of January 1700, *Nature*, *379*, 246–249, doi:10.1038/379246a0.

Tsuruoka, H., L. Rivera, H. Kawakatsu, and H. Kanamori (2009a), Real-time source inversion using W-phase and GRiD MT for regional tsunami early warning, *Eos Trans. AGU*, *90*(52), Fall Meet. Suppl., Abstract S13A-1732.

Tsuruoka, H., H. Kawakatsu, and T. Urabe (2009b), GRiD MT (grid-based real-time determination of moment tensors) monitoring the long-period seismic wavefield, *Phys. Earth Planet. Inter.*, *175*, 8–16, doi:10.1016/j.pepi.2008.02.014.

D. S. Dreger and A. Guilhem, Berkeley Seismological Laboratory, University of California, 225 McCone Hall, Berkeley, CA 94720-4670, USA. (aurelie@seismo.berkeley.edu)

Auxiliary material for paper 2011GL047550

Rapid detection and characterization of large earthquakes using quasi-finite-source Green's functions in continuous moment tensor inversion

Aurélie Guilhem and Douglas S. Dreger

Berkeley Seismological Laboratory, University of California, Berkeley, 225 McCone Hall, Berkeley, CA 94720-4670

Introduction

This auxiliary material contains a section called *Method* and another called *Additional Tests*, two tables, eight figures, and their figure captions.

Method

Green's functions: We used the frequency wave number integration method written by Chandan Saikia, FKRPROG [personal communication, 1994] to create a catalog of velocity Green's functions (GFs) for all the points of the grid and for the predefined set of seismic stations. They were computed using a 1D velocity model (GIL7) that is utilized for routine earthquake analyses in northern California [*Baise et al.*, 2003]. In this model, the MOHO depth is at 25 km.

Use of strong-motion records: Routine moment tensor inversions at the Berkeley Seismological Laboratory are performed using displacement seismograms. However, in order to avoid the integration from velocity to displacement in the realtime algorithm, we downloaded and inverted the velocity seismograms (LH channels) at the four selected seismic stations for testing purpose.

Similarly, the inversions for the M8+ events were also performed using velocity synthetic seismograms. Nonetheless for the realtime approach, we plan to use high-sampled (100 Hz) velocity channels (HH channels) at the four stations to invert for the source parameters of M3.5-to-7 earthquakes because of the short latency required. Regarding larger earthquakes along the CSZ, we propose to invert the strong-motion data (HL channels) to account for the strong shaking in the near-field. We verified that this approach was applicable for large events by comparing the real velocity seismograms obtained after integration of the strong-motion waveforms recorded at station MYG004 (K-NET) in Japan after the 2011 M9 earthquake to records modeled at YBH for a M9.1 and M8.5 earthquake along the CSZ. We found that even when the unfiltered real data demonstrate accelerations up to 3 g and show source-caused complexities, the long period filtered data are relatively simple and allow the correct detection and characterization of the event (Figures S3 and S4). The filtered acceleration records from the Japan earthquake are also sufficiently rich in low-frequency energy to be used directly in the proposed approach.

Additional tests

M9 earthquake: We used the finite-fault model (model 3) of *Shao et al.* [2011] of the recent 2011 M9.1 Japan earthquake and adapted it for the MTJ region (Figure S4). The resulting rupture segment is wider than other tested models (Figures 2, S1, S2). Its rupture extends downdip below most of the pre-selected seismic stations. Because of this downdip extension, the amplitudes of the strong-motion data are larger than expected compared to a Mw8.5 earthquake in the same region (Figure S3). Using the very long period (100-200 sec) velocity records of this

adapted Mw9.1 event and point-source GFs, we are able to correctly detect the occurrence of the large earthquake within 8 minutes, and to determine its centroid location, correct magnitude and focal mechanism (i.e. dip slip). Our best solution has a VR of 85%, indicating that such event would be very well detected by the proposed approach. The compactness of the slip is well represented by the point-source assumption (Figure S4). We expect that quasi-finite-source Green's functions could further improve the fit to the data.

Seismic noise: We also tested the approach on 630 seconds of seismic noise in which no local and teleseismic earthquakes were reported in the ANSS catalog. We recorded a maximum VR of 4.9 % and 22% for data filtered between 20 and 50 sec and between 100 and 200 sec, respectively. These VRs are well below a possible VR threshold that would be used for earthquake detection (for example 65% used in Japan [Tsuruoka et al., 2009b]) and no detection would have been made both at 20-50 sec and 100-200 sec periods. These best VRs yield Mw3 and Mw5 at the shorter and longer periods, respectively.

Passage of teleseismic waves in the study region: Another test was performed for the a 45 minute period following the 2009/03/19 M7.9 Tonga earthquake in which the major seismic energy of the earthquake travelled through the network with noticeable phase arrivals (P, S, and surface waves). For data filtered between 20 and 50 sec we found a maximum VR of 19.3%. However, the VR increased up to 56% for the 100-200 sec passband. This last solution shows that depending on the VR threshold used for earthquake detection, this teleseismic event could be falsely identified as a local/regional earthquake, however the magnitude is only 6.0 and

therefore could be excluded for additional consideration as an actual offshore great earthquake. Detections using the 100-200 sec passband should only be considered for M8+ earthquakes. Nonetheless, we found that the 20-50 sec passband gives satisfactory results for earthquakes with magnitude up to 7 located within the region (Figure 1 and Table S1).

Precision of the M8.4 earthquake inversion: The M8.4 earthquake results from the combination of two M8.2 earthquakes (Figure S2). Figure S2b shows that the best solutions at 14 km depth for the synthetic M8.4 earthquake are located slightly to the south of the main slip region of the southern rupture segment when using single-point GFs in a point-source moment tensor inversion. Also, in Figure S2 the main slip area of the northern segment is not well represented in the best VR map. This observation is found to be due to the interference of the waves originating from the two rupture zones. Indeed, we find that when we cancel out one of the segments we are able to correctly observe the other (Figure S7), with VRs up to 82%. In this case, the northern segment alone is better represented because of its larger distances from the seismic stations, which better satisfy the point-source assumption used in the moment tensor inversion. Another factor that is not considered in the point-source and the quasi-finite-source GFs is the change in strike of the rupture, which might also affect the results for the two segment rupture and interfering wave arrivals from each segment. However, we show that the single-strike quasi-finite-source GFs presented in Figure S2 appear as a good approximation for this earthquake and are generated using point-source GFs that are located in the main regions of slip of both fault segments.

Inferred rupture dimension of a large earthquake: Once an earthquake has been detected the approach may be extended by reviewing the time evolution of the moment tensor performance over the grid. Figure S8 shows that even if the VRs are low, it may be possible to determine the propagation of the large earthquake rupture and its extent from the spatial temporal distribution of high VR virtual sources. This behavior is similar to that of the back projection method of *Ishii et al.* [2007].

Reference (not included in the main text):

Baise, L . G., D. S. Dreger and S. D. Glaser (2003). The Effect of Shallow San Francisco Bay Sediments on Waveforms Recorded during the *M*W 4.6 Bolinas, California, Earthquake, Bull. Seism. Soc. Am., Vol. 93, No. 1, pp. 465–479.

Ishii, M., P. M. Shearer, H. Houston, and J. E. Vidale (2007), Teleseismic *P* wave imaging of the 26 December 2004 Sumatra-Andaman and 28 March 2005 Sumatra earthquake ruptures using the Hi-net array (2007), J. Geophys. Res., 112, B11307, doi:10.1029/2006JB004700

Supplementary Tables:

Table S1: Table of the source parameters obtained for the tested M4 to 7 earthquakes shown in Figure 1.

	ANSS catalog					Continuous moment tensor analysis									Differences			
Date	**Origin time**	**Lat**	**Lon**	**Depth**	**M**	**Origin time**	**Lat**	**Lon**	**Depth**	**Mw**	**Strike**	**Rake**	**Dip**	**VR**	**Horizontal distance (km)**	**Vertical distance (km)**	**Origin time**	**Magnitude**
8/15/2003	9:22:15	40.985	-125.43	8.6	5.3	9:22:16	41	-125.4	23	5.1	230	14	85	79.56	3	14.4	0:00:01	0.2
12/22/2004	20:47:27	42.479	-126.768	10	5.1	20:47:26	42.4	-126.8	38	5.1	18	-94	70	69.81	9.2	28	0:00:01	0
3/7/2005	2:34:34	42.512	-126.575	10	5.3	2:34:34	42.6	-126.6	38	5.2	328	-143	89	71.3	10	28	0:00:00	0.1
3/7/2005	2:48:20	42.534	-126.529	10	5.2	2:48:24	42.6	-126.4	38	5.1	145	145	89	73.82	12.9	28	0:00:04	0.1
6/15/2005	2:50:54	41.292	-125.953	16	7.2	2:51:12	41.4	-125.6	38	7	228	20	80	69.7	31.9	22	0:00:18	0.2
6/17/2005	6:21:43	40.773	-126.574	12	6.6	6:21:44	40.8	-126.6	38	6.6	107	165	81	75.93	3.7	26	0:00:01	0
3/22/2006	5:42:03	40.744	-126.319	10	5	5:42:08	41	-126.2	38	5	109	159	88	78.92	19.4	28	0:00:05	0
3/25/2006	3:16:05	41.749	-126.08	10	5.1	3:16:08	42	-126	26	4.9	349	-108	66	75.39	13.4	16	0:00:03	0.2
3/25/2006	20:14:07	41.983	-125.902	10	5	20:14:06	42	-126	32	4.9	32	-39	73	74.47	8.3	22	0:00:01	0.1
7/19/2006	11:41:43	40.2807	-124.433	20.69	5	11:41:50	40.4	-124.2	29	4.9	102	174	86	78.16	23.8	8.31	0:00:07	0.1
2/26/2007	12:19:54	40.6428	-124.866	0.01	5.4	12:19:56	40.6	-125	23	5.4	245	22	84	67.8	12.3	22.99	0:00:02	0
5/9/2007	7:50:04	40.3745	-125.016	0.17	5.2	7:50:04	40.4	-125.2	23	5.3	191	11	87	80.35	15.9	22.83	0:00:00	0.1
6/25/2007	2:32:25	41.1166	-124.825	3.36	5	2:32:32	41.2	-124.6	26	4.9	312	-170	89	84.68	21	22.64	0:00:07	0.1
3/15/2008	14:44:36	42.412	-126.835	10	5.7	14:44:40	42.4	-126.6	39	5.7	19	-92	68	70.32	19.4	29	0:00:04	0
4/30/2008	3:03:07	40.8358	-123.497	29.13	5.4	3:03:10	40.8	-123.4	35	5.3	5	-81	51	69.19	9.1	5.87	0:00:03	0.1
7/30/2008	13:39:34	40.4252	-125.33	18	4.2	13:39:38	40.6	-125.2	26	4.2	101	171	84	79.62	22.3	8	0:00:04	0
11/28/2008	13:42:19	40.348	-126.978	10	5.9	13:42:28	40.6	-126.6	38	5.9	270	-149	86	75.63	42.7	28	0:00:09	0
11/4/2009	2:16:56	40.4618	-125.6	15.5	4.17	2:16:50	40.4	-126	29	4.1	2	-27	71	70.67	34.6	13.5	0:00:06	0.07
1/10/2010	0:27:39	40.652	-124.693	29.33	6.5	0:27:48	40.6	-124.6	26	6.4	49	-31	85	58.53	9.7	3.33	0:00:09	0.1
2/4/2010	20:20:22	40.4123	-124.961	23.63	5.88	20:20:20	40.4	-125.2	23	5.8	217	10	83	79.43	20.3	0.63	0:00:02	0.08
4/15/2010	8:36:00	40.3515	-126.307	26.8	3.94	8:36:02	40.6	-126.2	38	4.5	274	-163	89	79.92	29.1	11.2	0:00:02	0.56
5/13/2010	5:35:12	42.263	-126.499	10	5.3	5:35:18	42.2	-126.2	35	5.2	13	-96	65	76.1	25.7	25	0:00:06	0.1
3/6/2011	13:46:38	40.4038	-125.363	24.73	4.5	13:46:42	40.6	-125.2	26	4.5	100	172	84	71.46	32.3	1.27	0:00:04	0

Table S2: Results for a variable slip model M8.2 reverse earthquake (Figure S4) and a synthetic M8.4 reverse earthquake (Figure S3). The best VRs are obtained for a South to North rupture that corresponds to the synthetic ruptures considered in the test. Time is given relative to the origin time of the synthetic earthquakes.

		1 point	3 points/ no delay	South to North	North to South	Bilateral
M8.2	VR (%)	66.53	71.69	75.12	66.78	72.69
	Time (sec)	+12	+6	-4	-4	0
	Mw	8.2	8.2	8.2	8.2	8.2
M8.4	VR (%)	58.05	46.12	68.22	11.05	47.96
	Time	+16	+20	0	0	-4
	Mw	8.1	8.2	8.3	8	8.3

Supplementary figures:

Figure S1: a) Map of grid points (dots) at 11 km depth color-coded by their best variance reduction for a modeled M8.2 earthquake with uniform slip (rectangle). The best solution shown by the black beach-ball diagram (center, VR=54.6%) at 100-200 sec period is compared to the input mechanism (red, left) and to the best solution (VR=47% for Mw6.7) obtained with the 20-50 sec passband (brown, right) . b) Unfiltered, 20-50 sec period, and 100-200 second period vertical component velocity waveforms at WDC for the fault rupture shown in a) are compared (back, solid traces). The point-source GFs in the respective passbands (red, dashed traces) are scaled by the scalar moment obtained from the respective moment tensor inversions shown a). Note that in the 20-50 second passband only a fraction of the time series is fit, whereas in the 100-200 second passband the same point-source Green's functions can fit most of the data.

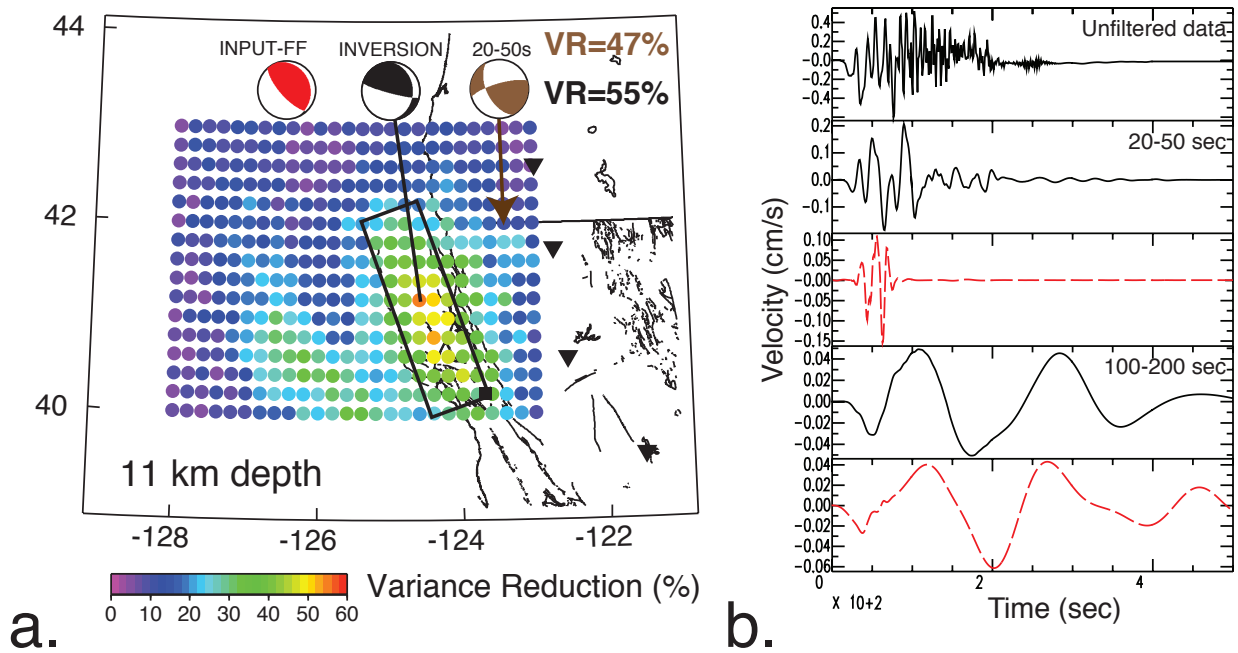

Figure S2: Test for a synthetic Mw8.4 earthquake. a) Slip model of the synthetic earthquake. INPUT-FF indicates the focal mechanisms (gray) of the input model that is composed of two M8 rupture (black square: rupture initiation). The gray region shows the area of the point-sources used in b). Triangles locate the four seismic stations. b) Best VRs at 14 km depth using single-point-source (SPS) GFs. The focal mechanism (black) of the best VR (58.05%) is shown and obtained 16 sec after the origin time of the synthetic test. c) Red circles shows the three points that are combined to generate composite GFs and to which a northward rupture is included. The VR increases to 67.84% (Table S2) and the mechanism (QFF) in black is very similar to the input mechanism.

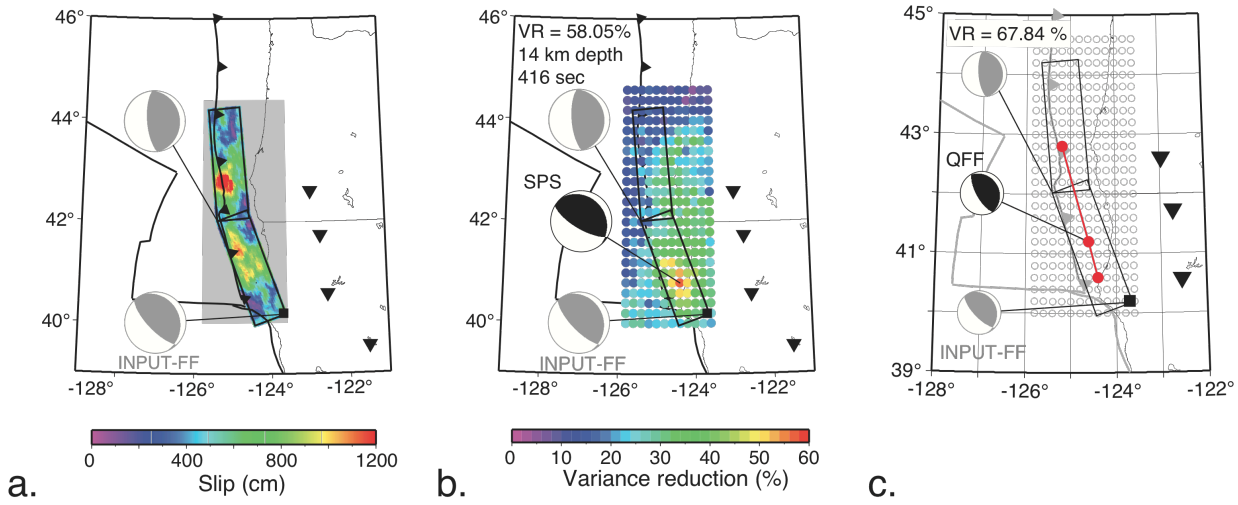

Figure S3: East-West unfiltered strong-motion record (acceleration, left), 100-200 sec integrated to velocity strong-motion data at MYG004 (K-NET) of the M9 Japan earthquake compared with East-West 100-200 sec velocity record at YBH for a synthetic M9 event offshore Mendocino (Figure S4), and a synthetic M8.4 earthquake (Figure S2), from left to right respectively. MYG004 is located about 175 km from the JMA location (294°/113° azimuth) and YBH is located about 143 km from synthetic hypocenter (101°/282° azimuth).

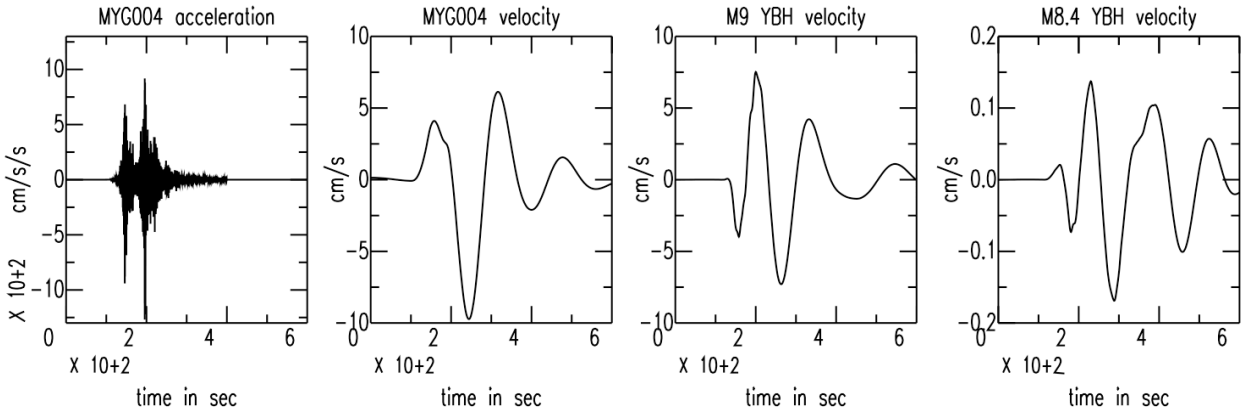

Figure S4: Simulation of the equivalent of the 2011 M9 Japan earthquake using *Shao et al.*'s [2011] slip model for the MTJ region (left) and map of the best VRs obtained between 75 sec before and 125 sec after the origin time of the earthquake (right). The input mechanism (INPUT) of the simulation is compared with the best solution from the very-long period single point source GFs (INVERSION). Our best solution is found with VR=85% and Mw9.1.

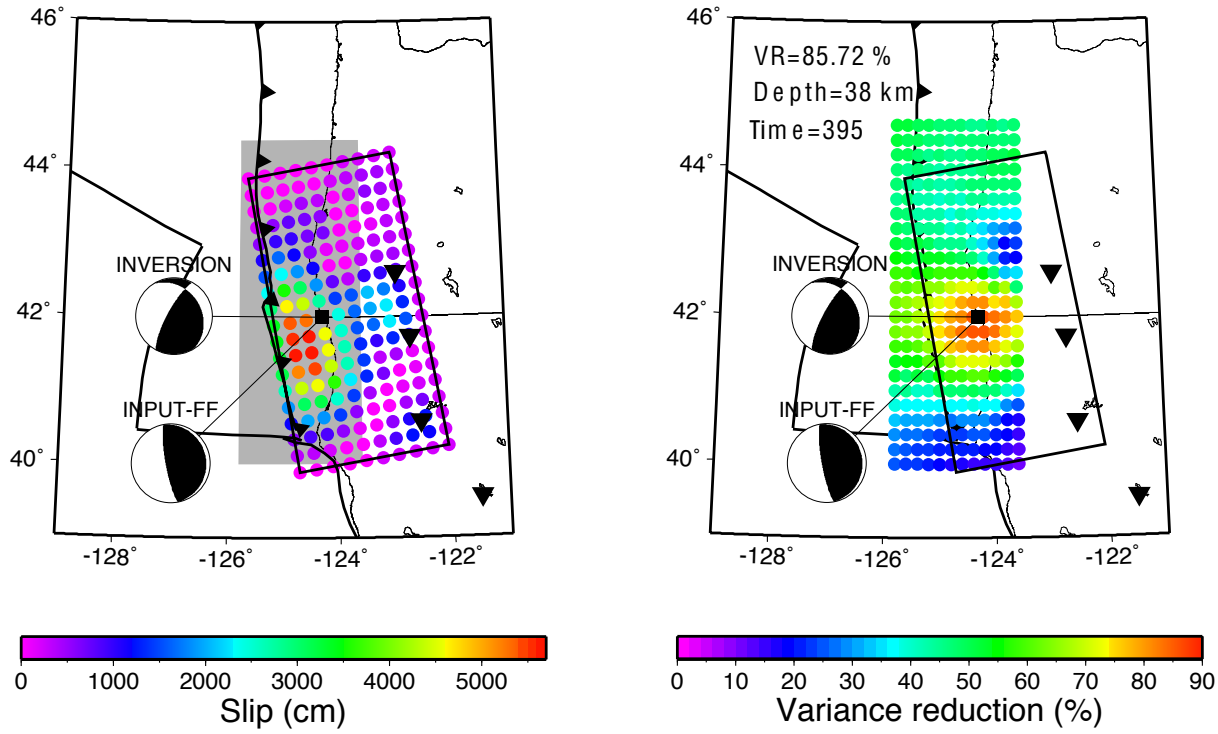

Figure S5: Mechanism stability test of the detection of a Mw5.0 earthquake. Missing components are modeled with amplitudes set at 0. Missing stations are not considered in the moment tensor inversion.

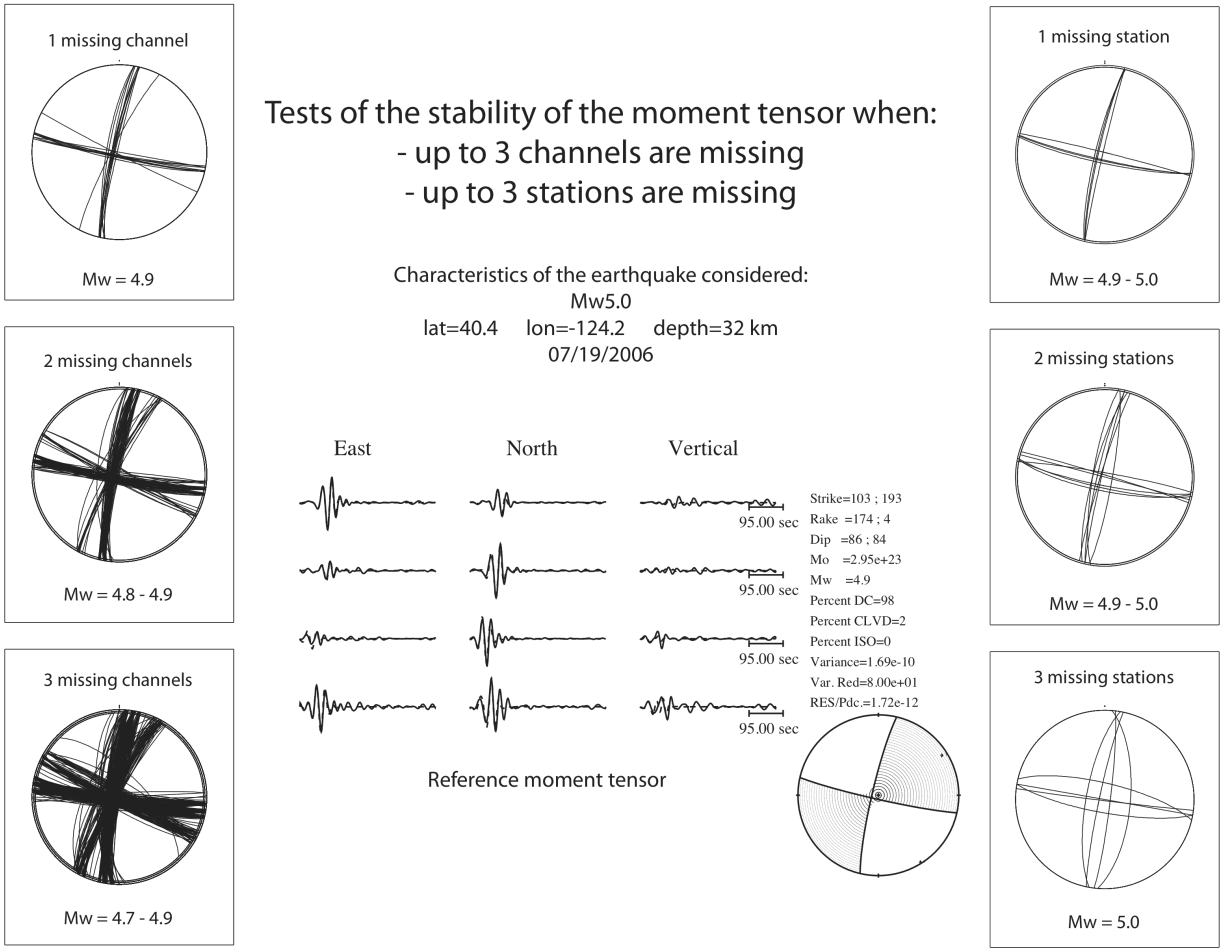

Figure S6: Effect of missing channels and stations on the detection of a Mw5.0 earthquake (Figure S5). a) Effect of missing from 1 to 3 components. Here, the missing component(s) is represented with a zero-amplitude trace and is considered in the calculation of the variance reduction. Significant reductions of the VR are observed indicating that the event could go under-detected in some cases. b) Effect of the number of stations considered in the moment tensor inversion. The missing station(s) is not considered in the calculation of the variance reduction. The missing stations have less influence on the detection of the earthquake than the components have (a).

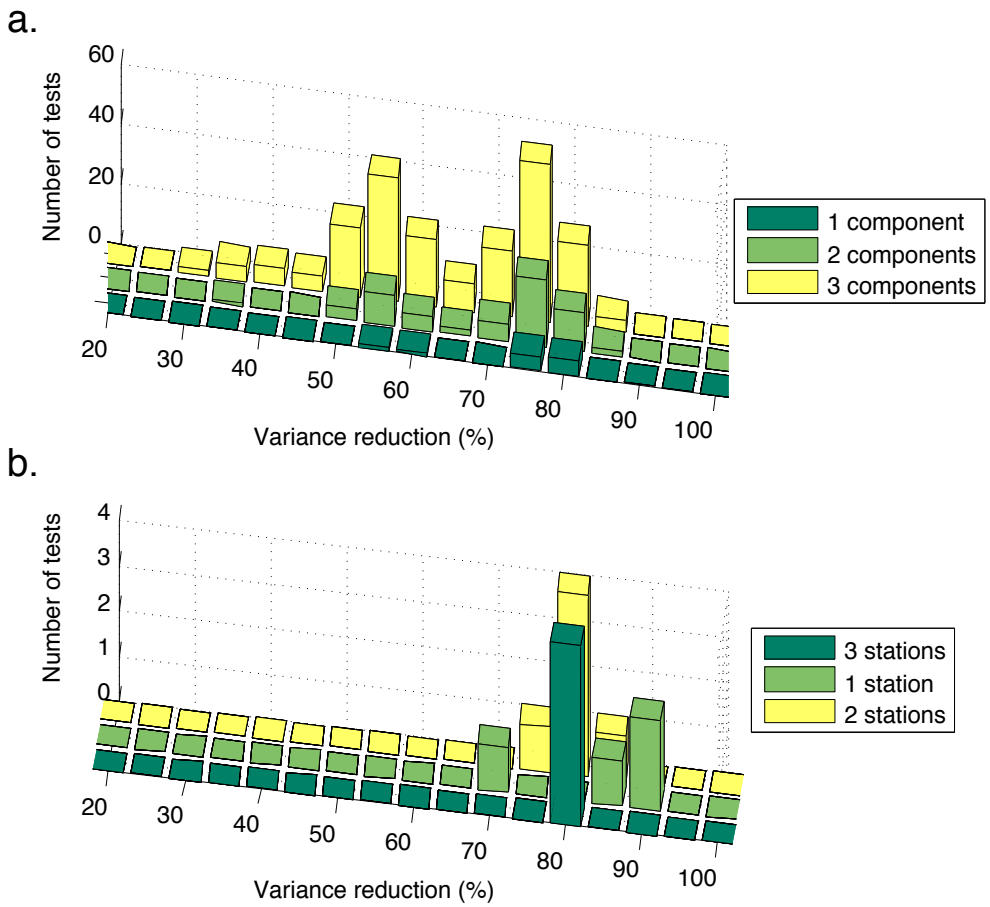

Figure S7: Influence of a compound fault rupture in the moment tensor inversion for a M8.4 earthquake (Figure S2). a) Slip model of the synthetic earthquake. INPUT-FF indicates the focal mechanisms in gray of the input model (black square: rupture initiation). The gray region shows the area of the point-sources used in b). Triangles locate the four seismic stations. b) Best VRs at 14 km depth using single-point-source (SPS) GFs for the test using the entire rupture. The focal mechanism (black) of the best VR (58.05%) is shown and obtained 16 sec after the origin time of the synthetic test. c) Best VRs at 14 km depth using single-point-source (SPS) GFs for the southern rupture only. The slip of the northern segment is fixed at 0. The focal mechanism (black) of the best VR (58.05%) is shown and obtained 16 sec after the origin time of the synthetic test. d) Best VRs at 14 km depth using single-point-source (SPS) GFs for the northern rupture only. The slip of the southern segment is fixed at 0. The focal mechanism (black) of the best VR (82.88%) is shown and obtained 16 sec after the origin time of the synthetic test.

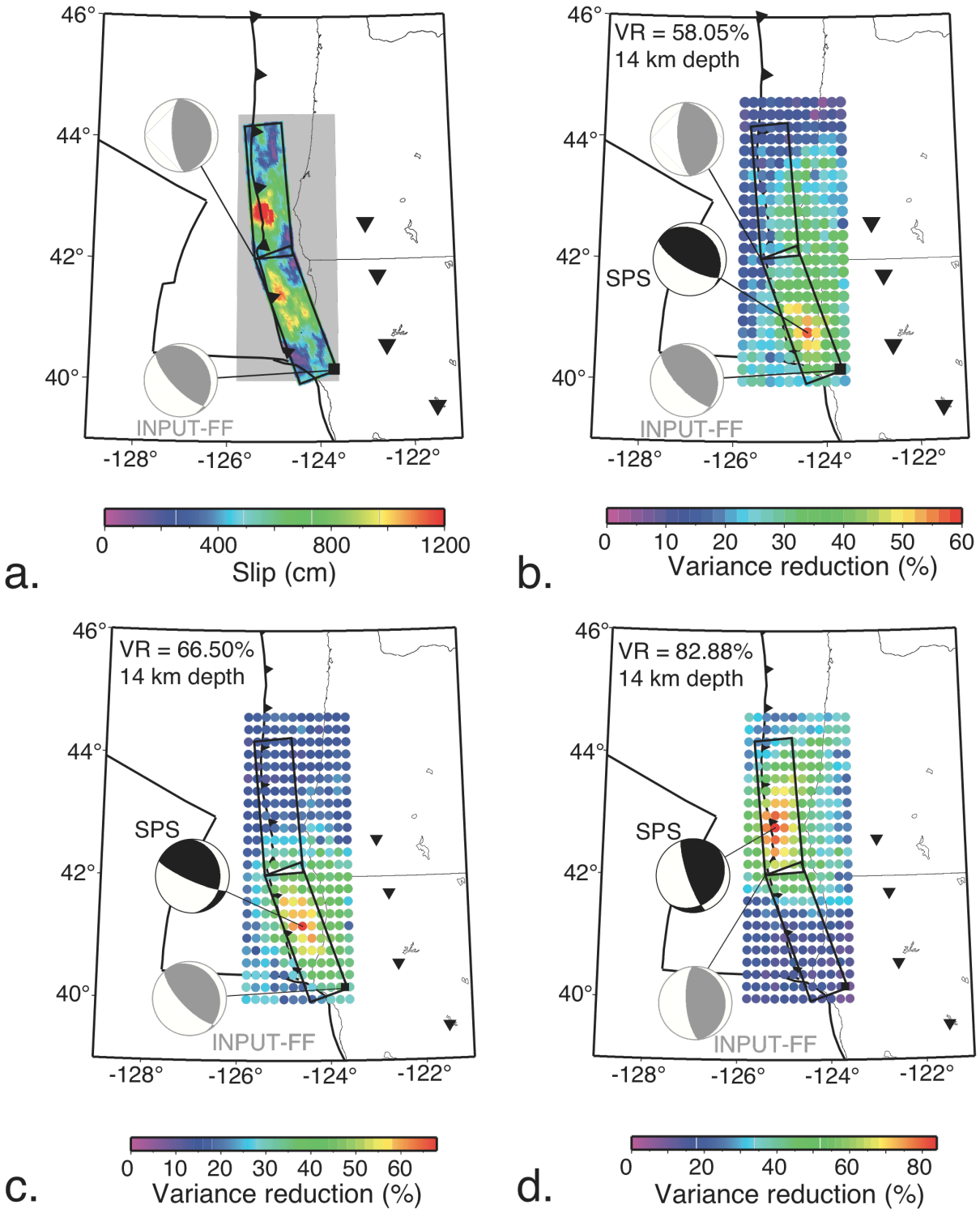
46°
44°
42°
40°
-128°
-126°
-124°
-122°
INPUT-FF
0
400
800
1200
Slip (cm)
a.
VR = 58.05%
14 km depth
SPS
INPUT-FF
0
10
20
30
40
50
60
Variance reduction (%)
b.
VR = 66.50%
14 km depth
SPS
INPUT-FF
0
10
20
30
40
50
60
Variance reduction (%)
c.
VR = 82.88%
14 km depth
SPS
INPUT-FF
0
20
40
60
80
Variance reduction (%)
d.
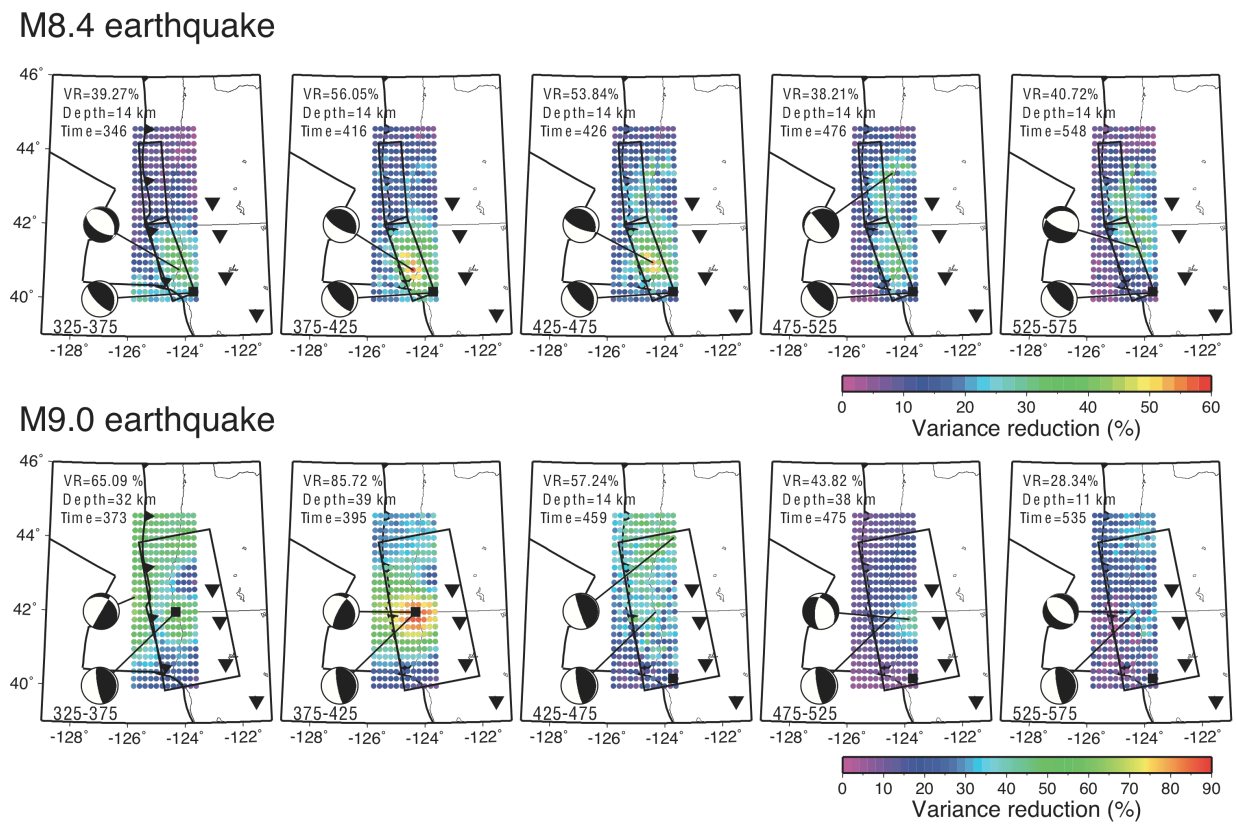
Figure S8: Time evolution of the best detections of a M8.4 earthquake (top) and for a M9.0 earthquake (bottom). The different maps show snapshots of the best VRs over the grid using point-source GFs for different time windows. Here, the origin time of the earthquake is at 400 sec. The bottom mechanism shows the input mechanism for the synthetic earthquakes and the top one shows the best solution from the inversion for the corresponding time.